Kinetics of Monolayer MoS_2 encapsulated Nanobubbles on Hexagonal Boron Nitride Substrates

Zihan Liu,[1] Yingchun Jiang,[1] Dingli Wang,[1] Junpeng Lai,[1] Huimin Zhou,[2] Jia Deng,[2] Changhong Ke[1,3*]

[1.] Department of Mechanical Engineering, State University of New York at Binghamton, Binghamton, NY 13902, USA

[2.] Department of Systems Science and Industrial Engineering, State University of New York at Binghamton, Binghamton, NY 13902, USA

[3.] Materials Science and Engineering Program, State University of New York at Binghamton, Binghamton, NY 13902, USA

*To whom correspondence should be addressed: cke@binghamton.edu

Abstract

Understanding the kinetics of nanobubbles encapsulated by ultrathin two-dimensional (2D) layered van der Waals crystal membranes on atomically flat substrates is important to the applications of 2D materials and the pursuit of 2D nanobubble technologies. Here, we investigate the controlled motion of monolayer molybdenum disulfide (MoS_2) encapsulated nanobubbles on flat hexagonal boron nitride (hBN) substrates using atomic force microscopy (AFM). Our study reveals a distinct transition from standstill bubble deformations to stable, stepwise bubble translations on flat substrates. The membrane tension-dominated 2D nanobubble behaves like an elastic soft body in its collision interaction with the AFM tip. This delicate motion-control technique enables neighboring 2D nanobubbles to move closer and eventually coalesce into larger

nanobubbles. These findings pave the way for high-precision manipulation of nanobubbles and facilitate the exploration of their emerging applications.

Keywords: *2D materials, nanobubbles, kinetics, atomic force microscopy, friction*

The extraordinary physical and chemical properties of two-dimensional (2D) layered crystal materials-based electronics and sensors[1] often critically rely on an intimate van der Waals interface[2–6] with either a traditional substrate (e.g., silicon dioxide) or a substrate made of 2D materials (either homo- or heterogeneous types[7–9]). Nanobubbles reportedly form between the 2D membrane and the substrate, particularly during the 2D transfer process by encapsulating the ambient moisture, gas, and/or absorbed surface contaminants. The spontaneously formed nanobubbles, which are reportedly hard to avoid,[10,11] can lead to significant charge inhomogeneity and reduced carrier mobility,[12] negatively impacting the performance of 2D electronics. On the other hand, the formation of nanobubbles indicates decent adhesion between the 2D membrane and the substrate[13,14]. This can be utilized as a strategy for self-cleaning the substrate[15,16] and tuning the mechanical strain in the 2D membrane (i.e., strain engineering).[17,18] The interface-confined small volume between the 2D membrane and the substrate, in the order of *femto*- to *yoctoliters*, opens a pathway as emerging carriers of minuscule amounts of mass, drug, and biomolecules.[19–21] From a structural perspective, the formation of the 2D membrane-encapsulated nanobubble involves a complex interplay of adhesion, internal pressure, and membrane straining, which has been extensively studied in recent years.[22–25] Understanding and ultimately controlling the motion of the 2D nanobubble will create opportunities for the optimal design and performance of 2D devices by eliminating nanobubbles and pursuing emerging applications of 2D nanobubbles (e.g.,

drug delivery).[26] However, the kinetics of 2D nanobubbles, particularly those encapsulated between ultrathin (mono- or few-layer) 2D membranes on atomically flat substrates, remain elusive. In this letter, we investigate the controlled motion of monolayer molybdenum disulfide (MoS_2) encapsulated nanobubbles on atomically flat hexagonal boron nitride (hBN) substrates using atomic force microscopy (AFM). MoS_2 is a type of semiconductive transition metal dichalcogenide (TMD) with superior mechanical properties[27] and electron mobilities,[28] and is a promising building block for next-generation nanoelectronics and optoelectronics, while hBN is an excellent insulator for 2D electronics, including those made of MoS_2.[29,30] The bending stiffness of MoS_2 scales approximately with the square of its thickness (or the number of layers),[27] while its tensile modulus scales linearly with its thickness. Therefore, the low bending stiffness of monolayer MoS_2 enables it to conform well to the flat substrate and the trapped medium, and the in-plane stretching effect in the ultrathin bubble membrane plays a most dominant role in bubble formation. Our AFM measurements of MoS_2-encapsulated nanobubbles on flat hBN substrates reveal a distinct transition from standstill bubble deformations to stable, stepwise bubble translations and the complex AFM tip-bubble interactions in bubble deformation and motion.

Figure 1(a) shows MoS_2/hBN-encapsulated nanobubbles formed during an all-dry transfer process[31] under ambient environments (~23°C; relative humidity ~20%) (see the *Supplementary Material* for materials and methods). The exhibited MoS_2 flake possesses two thickness domains: monolayer and bilayer (1L and 2L), which are determined based on AFM height and Raman measurements[32] (Fig. S1 in the *Supplementary Material*). The measured thickness of 1L MoS_2 (~0.634 nm) on the hBN surface is close to its theoretical value (~0.615 nm),[33] which indicates a clean surface that is free of polymer residues or other surface contaminants. The nanobubbles are circular with a dispersed size distribution. Topography measurements of nanobubbles

encapsulated by monolayer MoS_2, using non-contact mode AFM with a silicon cantilever of 10 nm nominal tip radius, show bubble radii (a) in the range of 95 to 362 nm and bubble heights (h) in the range of 14 to 54 nm, yielding a bubble height-to-radius ratio (h/a) of 0.12 to 0.15. Fig. 1(b) illustrates the nanobubble manipulation inside a Park System XE-70 AFM that operates in the lateral force mode. The AFM measurements were conducted using CSG 10 AFM cantilevers (NT-MDT) with a nominal tip radius ~10 nm and individually calibrated normal spring constant ~0.2-0.6 N/m using the Sader Method.[34] The lateral force applied to the AFM tip is calculated based on the torsional sensitivity coefficient of the AFM cantilever, which is found within the range of 0.039-0.110 nN/mV using a two-slope wedge method.[35] During the bubble manipulation experiment, the AFM tip is controlled to scan unidirectionally through the bubble centerline to characterize the bubble deformation and the AFM tip-bubble interaction force under each scan.

The blue-dashed curve in Fig. 1(c) shows the topography profile of a representative 1L-MoS_2/hBN encapsulated nanobubble with a height of ~37 nm obtained via non-contact mode AFM imaging. A lateral-mode AFM scan with a normal load of 1 nN and a scan rate of 500 nm/s reduced the bubble height to ~31 nm (black-solid curve in Fig. 1(c)). The bubble remained at a standstill on the substrate during the AFM scan, and its deformation was fully reversible. Fig. 1(d) shows the corresponding lateral force interaction as the AFM tip slid over the 2D bubble surface, which can be categorized into three stages: *climbing*, *plateau*, and *descending*. Once in lateral collision contact with the bubble, the AFM tip indents and slides up along the bubble surface, which is exhibited as a sharp increase in the lateral interaction force. The measured lateral force when the AFM tip reaches the top of the bubble membrane indicates the frictional force between the AFM tip and the bubble membrane (~5 nN), which more than doubles the friction force (~2.3 nN) in the flat MoS_2/hBN contact region. Our AFM measurements show that the MoS_2 surface on top of the

nanobubble possesses a much lower surface roughness (0.22 ± 0.03 nm) than that in the flat MoS_2/hBN contact region (0.29±0.04 nm). The stretching-induced smoother 2D membrane surface is expected to result in a lower frictional force.[36] Therefore, the observed higher friction force between the AFM tip and the bubble membrane can be attributed to the partial *sink-in* of the AFM tip onto the bubble membrane, which increases the resistance to the motion of the AFM tip. The descending trace of the AFM tip squeezes the bubble membrane to form puckered structures.[37] The puckered structures act as roadblocks to the moving AFM tip, which increases the lateral interaction force as the AFM tip slides down the bubble surface. AFM imaging shows that the nanobubble's geometry (shape and size) and position remain intact after the AFM scan. The observed reversibility of the substantial bubble deformation indicates that the 2D bubble behaves like an elastic soft body.

Figs. 2(a, b) and 2(c) show the selected AFM topographic and lateral force measurements, respectively, of the bubble in Fig. 1(c) under normal loads of up to 30 nN. The measurements reveal that the bubble remains at a standstill on the substrate with the applied normal load reaching up to 20 nN. The bubble starts to move in a unidirectional *forward* translation mode (i.e., along the scan direction of the AFM tip) under a normal load of 25 nN (Fig. 2(a)), as indicated by the shift of the bubble's center position. Here, the bubble's center position is considered to coincide with the position of its peak height (h) in the measured topography profile, which is determined by a quadratic curve fitting (see Fig. S2). The forward translation of the bubble continues for the first three scans under a normal load of 30 nN, and then the bubble is observed to move in both forward and transverse directions for the last two scans (Fig. 2(b) and the insert AFM image). The peak lateral collision force is found to vary linearly with the normal load (blue curve in Fig. 2(d)).[38,39] Additionally, the bubble's transverse size (diameter) and height remain intact after all

these AFM measurements. Fig. 2(d) shows the center position of the nanobubble under each AFM scan (black curve in Fig. 2(d)). The bubble moves, in a rather uniform and stepwise manner, by a distance of 14 to 18 nm for scans under a normal load of 25 nN. The translation distance increases to the range of 19 to 50 nm under a normal load of 30 nN. The results show a general trend that the bubble travels a longer distance on the flat substrate under a higher normal load, which can be attributed to the resulting higher lateral collision force. Meanwhile, it also leads to a greater deviation in the moving step size. The observed scattering of the moving step size for scans even under the same normal load (30 nN) can be attributed to the variation in the AFM scan pathway due to the thermal shift of the AFM scanning stages.[40] This is evidenced by the observed transverse motions of the bubble during the fourth and fifth scans under a load of 30 nN (Fig. 2(b)), which indicates that the scan pathway of the AFM tip deviates from the bubble's centerline. The detailed topographic and lateral force evolution for the bubble under normal loads of 25 nN and 30 nN are shown in Fig. S3.

The bubble's movability on a flat substrate is governed by the interplay of several factors, including the applied normal load and the resulting AFM tip-bubble lateral and frictional forces, the AFM tip scan speed, and the geometry of the bubble. Fig. 3(a) shows the correlation between the applied normal load and the resulting lateral collision force that was recorded on the same bubble in Fig. 1(c) for varying AFM tip scan speeds within the range of 50-2000 nm/s. The shaded region in Fig. 3(a) indicates the bubble's movable region. The data show that an increasing AFM tip scan speed results in a higher lateral collision force under the same normal load. The normal load threshold that initiates the bubble motion increases with the AFM tip scan velocity. Fig. 3(b) shows that the average moving distance of the bubble under each AFM scan increases with the applied normal load but decreases with an increase in the AFM tip scan speed. The results

consistently show that, under a certain applied normal load, the bubble is prone to move by using a slow-moving AFM tip. Fig. 3(c) shows the dependence of the AFM tip-bubble friction force that was recorded when the AFM tip slides atop the bubble surface. The friction force increases with the applied normal load and the AFM tip scan speed, which is consistent with previous reports on the frictional behavior of monolayer and bulk MoS_2 surface.[41] The frictional force data could be well-fitted using a power function given by $f = C \times (P + A_{bt})^{2/3}$, in which A_{bt} is the adhesion force between the AFM tip and the MoS_2 bubble, P is the applied normal load, and C is a fitting parameter. For the tested MoS_2 bubbles, the adhesion force A_{bt} was measured to be about 7.09 ± 0.54 nN from the force-distance spectroscopy measurement (Fig. S4). The measured AFM tip-bubble frictional force is noticeably higher than the friction force in the flat MoS_2/hBN region (Fig. S5), which indicates that the deformability of the MoS_2 membrane helps engage the lateral/frictional interaction with the AFM tip. We conducted AFM measurements on nine monolayer MoS_2/hBN-encapsulated nanobubbles with a varying bubble radius, ranging from 95 to 362 nm, while maintaining a consistent aspect ratio (h/a) of ~0.14. Fig. 3(d) shows the lateral collision force threshold to initiate the bubble motion follows a linearly proportional dependence on the bubble radius. The results show that the required normal and lateral collision forces to move the bubble scale with the bubble size.

The AFM-based 2D nanobubble manipulation approach reported here enables the merging of neighboring 2D bubbles to form a larger bubble. The selected AFM images in Fig. 4(a) show the process of merging two 1L-MoS_2 bubbles about 1 μm apart by moving one of the bubbles to approach and eventually coalesce with the other bubble. The AFM topographic profiles in Fig. 4(b) show that the two bubbles in Fig. 4(a) are of radius (height) ~139.8 nm (19.7nm) and ~144.5 nm (20.5 nm), respectively. The newly formed bubble has a radius of ~175.5 nm and a height of

~26.6 nm. The h/a ratio of the newly formed bubble (~0.152) noticeably increases compared to that of the original bubbles (~0.141-0.142). Here, we examine the potential impact of the change in the h/a ratio on the confinement pressure inside the bubble and the mechanical strain inside the bubble membrane. The confinement pressure is given as $\Delta p \approx Et\frac{2}{1-\nu}\frac{h^3}{a^4}$, [ref. 25] where E, t and ν are the Young's modulus, thickness, and Poisson's ratio of the bubble membrane (E = 330 GPa,[42] t=0.615 nm[33] and ν = 0.25[43] for monolayer MoS_2), respectively. Our analysis shows that the pressure inside the newly formed bubble (~10.7 MPa) remains almost unchanged as compared to that in the original bubbles (~10.7 MPa and ~10.8 MPa). The low bending stiffness of 1L MoS_2 and the tension-dominated MoS_2 bubble membrane help the bubble maintain its structural stability.

The mechanical strain inside the bubble membrane can be estimated using the Föppl–von Kármán equation.[44] If the edge of the bubble is assumed to be fully clamped at the bubble-substrate interface, the radial (ϵ_r) and circumferential (ϵ_θ) strains inside the bubble membrane are given as $\epsilon_r = \frac{h^2}{4a^2}(3-\nu)\left[1-\frac{1-3\nu}{3-\nu}\left(\frac{r}{a}\right)^2\right]$ and $\epsilon_\theta = \frac{h^2}{4a^2}(3-\nu)\left[1-\left(\frac{r}{a}\right)^2\right]$, respectively, where ν is the Poisson's ratio of the bubble membrane and r is the radial coordinate. The maximum strain occurs at the top position of the bubble (r = 0), in which the corresponding strain is given as $\epsilon_r(r=0) = \epsilon_\theta(r=0) = \frac{h^2}{4a^2}(3-\nu)$. For the bubbles exhibited in Fig. 4(a), the maximum strain in the newly formed bubble (~1.58%) is about 13.5-15.6% higher than that in the original bubbles (~1.36-1.39%). The findings suggest that the bubble merging process presents a plausible approach for strain-engineering of 2D materials.

In summary, we investigated the precisely controlled motion of ultrathin MoS_2-encapsulated nanobubbles on flat hBN substrates. Our study reveals the distinct transition from standstill bubble deformations to stable stepwise bubble translation and how the deformation and motion of the 2D

bubble are governed by the complex AFM tip-bubble collision interactions. The bubble behaves like an elastic soft body and can maintain its size and shape after the controlled motion. The controlled merging of neighboring bubbles to form a larger bubble was demonstrated, which is accompanied by changes in the mechanical strain inside the 2D membrane. These findings pave the way for high-precision manipulation of nanobubbles and the exploration of their emerging applications.

Supplementary Material

See supplementary material for additional details about the experimental methods, and additional figures about the AFM and Raman measurements of the 2D materials, adhesion, bubble motion experiments, and friction.

Acknowledgments

The authors acknowledge the support of the National Science Foundation under grant nos. CMMI 2009134 and 2006127.

References

[1] S. Das, A. Sebastian, E. Pop, C.J. McClellan, A.D. Franklin, T. Grasser, T. Knobloch, Y. Illarionov, A.V. Penumatcha, J. Appenzeller, Z. Chen, W. Zhu, I. Asselberghs, L.-J. Li, U.E. Avci, N. Bhat, T.D. Anthopoulos, and R. Singh, "Transistors based on two-dimensional materials for future integrated circuits," Nat Electron **4**(11), 786–799 (2021).

[2] D. Jariwala, T.J. Marks, and M.C. Hersam, "Mixed-dimensional van der Waals heterostructures," Nature Mater **16**(2), 170–181 (2017).

[3] Y. Liu, N.O. Weiss, X. Duan, H.-C. Cheng, Y. Huang, and X. Duan, "Van der Waals heterostructures and devices," Nat Rev Mater **1**(9), 1–17 (2016).

[4] D.G. Purdie, N.M. Pugno, T. Taniguchi, K. Watanabe, A.C. Ferrari, and A. Lombardo, "Cleaning interfaces in layered materials heterostructures," Nat Commun **9**(1), 5387 (2018).

[5] S. Toyoda, T. Uwanno, T. Taniguchi, K. Watanabe, and K. Nagashio, "Pinpoint pick-up and bubble-free assembly of 2D materials using PDMS/PMMA polymers with lens shapes," Appl. Phys. Express **12**(5), 055008 (2019).

[6] F. Pizzocchero, L. Gammelgaard, B.S. Jessen, J.M. Caridad, L. Wang, J. Hone, P. Bøggild, and T.J. Booth, "The hot pick-up technique for batch assembly of van der Waals heterostructures," Nat Commun **7**(1), 11894 (2016).

[7] C.R. Dean, A.F. Young, I. Meric, C. Lee, L. Wang, S. Sorgenfrei, K. Watanabe, T. Taniguchi, P. Kim, K.L. Shepard, and J. Hone, "Boron nitride substrates for high-quality graphene electronics," Nat Nano **5**(10), 722–726 (2010).

[8] C. Dean, A.F. Young, L. Wang, I. Meric, G.-H. Lee, K. Watanabe, T. Taniguchi, K. Shepard, P. Kim, and J. Hone, "Graphene based heterostructures," Solid State Communications **152**(15), 1275–1282 (2012).

[9] Y. Cao, V. Fatemi, S. Fang, K. Watanabe, T. Taniguchi, E. Kaxiras, and P. Jarillo-Herrero, "Unconventional superconductivity in magic-angle graphene superlattices," Nature **556**(7699), 43–50 (2018).

[10] A. Jain, P. Bharadwaj, S. Heeg, M. Parzefall, T. Taniguchi, K. Watanabe, and L. Novotny, "Minimizing residues and strain in 2D materials transferred from PDMS," Nanotechnology **29**(26), 265203 (2018).

[11] A.V. Kretinin, Y. Cao, J.S. Tu, G.L. Yu, R. Jalil, K.S. Novoselov, S.J. Haigh, A. Gholinia, A. Mishchenko, M. Lozada, T. Georgiou, C.R. Woods, F. Withers, P. Blake, G. Eda, A. Wirsig, C. Hucho, K. Watanabe, T. Taniguchi, A.K. Geim, and R.V. Gorbachev, "Electronic Properties of Graphene Encapsulated with Different Two-Dimensional Atomic Crystals," Nano Lett. **14**(6), 3270–3276 (2014).

[12] Q.A. Vu, S. Fan, S.H. Lee, M.-K. Joo, W.J. Yu, and Y.H. Lee, "Near-zero hysteresis and near-ideal subthreshold swing in h-BN encapsulated single-layer MoS2 field-effect transistors," 2D Mater. **5**(3), 031001 (2018).

[13] N.G. Boddeti, X. Liu, R. Long, J. Xiao, J.S. Bunch, and M.L. Dunn, "Graphene Blisters with Switchable Shapes Controlled by Pressure and Adhesion," Nano Lett. **13**(12), 6216–6221 (2013).

[14] Z. Zong, C.-L. Chen, M.R. Dokmeci, and K. Wan, "Direct measurement of graphene adhesion on silicon surface by intercalation of nanoparticles," Journal of Applied Physics **107**(2), 026104 (2010).

[15] K.S. Novoselov, A. Mishchenko, A. Carvalho, and A.H. Castro Neto, "2D materials and van der Waals heterostructures," Science **353**(6298), aac9439 (2016).

[16] Y. Hou, Z. Dai, S. Zhang, S. Feng, G. Wang, L. Liu, Z. Xu, Q. Li, and Z. Zhang, "Elastocapillary cleaning of twisted bilayer graphene interfaces," Nat Commun **12**(1), 5069 (2021).

[17] A. Castellanos-Gomez, R. Roldán, E. Cappelluti, M. Buscema, F. Guinea, H.S.J. van der Zant, and G.A. Steele, "Local strain engineering in atomically thin MoS2," Nano Lett **13**(11), 5361–5366 (2013).

[18] D.A. Sanchez, Z. Dai, and N. Lu, "2D Material Bubbles: Fabrication, Characterization, and Applications," Trends in Chemistry **3**(3), 204–217 (2021).

[19] D. Tedeschi, E. Blundo, M. Felici, G. Pettinari, B. Liu, T. Yildrim, E. Petroni, C. Zhang, Y. Zhu, S. Sennato, Y. Lu, and A. Polimeni, "Controlled Micro/Nanodome Formation in Proton-Irradiated Bulk Transition-Metal Dichalcogenides," Advanced Materials **31**(44), 1903795 (2019).

[20] L. He, H. Wang, L. Chen, X. Wang, H. Xie, C. Jiang, C. Li, K. Elibol, J. Meyer, K. Watanabe, T. Taniguchi, Z. Wu, W. Wang, Z. Ni, X. Miao, C. Zhang, D. Zhang, H. Wang, and X. Xie, "Isolating hydrogen in hexagonal boron nitride bubbles by a plasma treatment," Nat Commun **10**(1), 2815 (2019).

[21] C. Herbig, E.H. Åhlgren, U.A. Schröder, A.J. Martínez-Galera, M.A. Arman, J. Kotakoski, J. Knudsen, A.V. Krasheninnikov, and T. Michely, "Xe irradiation of graphene on Ir(111): From trapping to blistering," Phys. Rev. B **92**(8), 085429 (2015).

[22] Z. Dai, N. Lu, K.M. Liechti, and R. Huang, "Mechanics at the interfaces of 2D materials: Challenges and opportunities," Current Opinion in Solid State and Materials Science **24**(4), 100837 (2020).

[23] Z. Dai, Y. Hou, D.A. Sanchez, G. Wang, C.J. Brennan, Z. Zhang, L. Liu, and N. Lu, "Interface-Governed Deformation of Nanobubbles and Nanotents Formed by Two-Dimensional Materials," Phys. Rev. Lett. **121**(26), 266101 (2018).

[24] E. Blundo, T. Yildirim, G. Pettinari, and A. Polimeni, "Experimental Adhesion Energy in van der Waals Crystals and Heterostructures from Atomically Thin Bubbles," Phys. Rev. Lett. **127**(4), 046101 (2021).

[25] D.A. Sanchez, Z. Dai, P. Wang, A. Cantu-Chavez, C.J. Brennan, R. Huang, and N. Lu, "Mechanics of spontaneously formed nanoblisters trapped by transferred 2D crystals," Proceedings of the National Academy of Sciences **115**(31), 7884–7889 (2018).

[26] L. Peng, X. Mei, J. He, J. Xu, W. Zhang, R. Liang, M. Wei, D.G. Evans, and X. Duan, "Monolayer Nanosheets with an Extremely High Drug Loading toward Controlled Delivery and Cancer Theranostics," Advanced Materials **30**(16), 1707389 (2018).

[27] Y. Jiang, S. Sridhar, Z. Liu, D. Wang, H. Zhou, J. Deng, H.B. Chew, and C. Ke, "The interplay of intra- and inter-layer interactions in bending rigidity of ultrathin 2D materials," Applied Physics Letters **122**(15), 153101 (2023).

[28] B. Radisavljevic, A. Radenovic, J. Brivio, V. Giacometti, and A. Kis, "Single-layer MoS2 transistors," Nature Nanotech **6**(3), 147–150 (2011).

[29] M. Sup Choi, G.-H. Lee, Y.-J. Yu, D.-Y. Lee, S. Hwan Lee, P. Kim, J. Hone, and W. Jong Yoo, "Controlled charge trapping by molybdenum disulphide and graphene in ultrathin heterostructured memory devices," Nat Commun **4**(1), 1624 (2013).

[30] G.-H. Lee, Y.-J. Yu, X. Cui, N. Petrone, C.-H. Lee, M.S. Choi, D.-Y. Lee, C. Lee, W.J. Yoo, K. Watanabe, T. Taniguchi, C. Nuckolls, P. Kim, and J. Hone, "Flexible and Transparent MoS2 Field-Effect Transistors on Hexagonal Boron Nitride-Graphene Heterostructures," ACS Nano **7**(9), 7931–7936 (2013).

[31] A. Castellanos-Gomez, M. Buscema, R. Molenaar, V. Singh, L. Janssen, H.S.J. van der Zant, and G.A. Steele, "Deterministic transfer of two-dimensional materials by all-dry viscoelastic stamping," 2D Mater. **1**(1), 011002 (2014).

[32] Y. Jiang, Z. Liu, H. Zhou, A. Sharma, J. Deng, and C. Ke, "Physical adsorption and oxidation of ultra-thin MoS2 crystals: insights into surface engineering for 2D electronics and beyond," Nanotechnology **34**(40), 405701 (2023).

[33] R.F. Frindt, "Single Crystals of MoS2 Several Molecular Layers Thick," Journal of Applied Physics **37**(4), 1928–1929 (1966).

[34] J.E. Sader, J.W.M. Chon, and P. Mulvaney, "Calibration of rectangular atomic force microscope cantilevers," Review of Scientific Instruments **70**(10), 3967–3969 (1999).

[35] D.F. Ogletree, R.W. Carpick, and M. Salmeron, "Calibration of frictional forces in atomic force microscopy," Review of Scientific Instruments **67**(9), 3298–3306 (1996).

[36] S. Zhang, Y. Hou, S. Li, L. Liu, Z. Zhang, X.-Q. Feng, and Q. Li, "Tuning friction to a superlubric state via in-plane straining," Proceedings of the National Academy of Sciences **116**(49), 24452–24456 (2019).

[37] M. Xu, D. Zhang, Y. Wang, Y. Zhang, Q. Li, and M. Dong, "Nanoscale friction of strained molybdenum disulfide induced by nanoblisters," Applied Physics Letters **120**(15), 151601 (2022).

[38] X. Chen, M. Zheng, C. Park, and C. Ke, "Collision and dynamic frictional properties of boron nitride nanotubes," Appl. Phys. Lett. **102**(12), 121912 (2013).

[39] M. Zheng, X. Chen, C. Park, C.C. Fay, N.M. Pugno, and C. Ke, "Nanomechanical cutting of boron nitride nanotubes by atomic force microscopy," Nanotechnology **24**(50), 505719 (2013).

[40] F. Marinello, P. Bariani, S. Carmignato, and E. Savio, "Geometrical modelling of scanning probe microscopes and characterization of errors," Meas. Sci. Technol. **20**(8), 084013 (2009).

[41] O. Acikgoz, and M.Z. Baykara, "Speed dependence of friction on single-layer and bulk MoS2 measured by atomic force microscopy," Applied Physics Letters **116**(7), 071603 (2020).

[42] A. Castellanos-Gomez, M. Poot, G.A. Steele, H.S.J. van der Zant, N. Agraït, and G. Rubio-Bollinger, "Elastic Properties of Freely Suspended MoS2 Nanosheets," Advanced Materials **24**(6), 772–775 (2012).

[43] Q. Yue, J. Kang, Z. Shao, X. Zhang, S. Chang, G. Wang, S. Qin, and J. Li, "Mechanical and electronic properties of monolayer MoS2 under elastic strain," Physics Letters A **376**(12), 1166–1170 (2012).

[44] L.B. Freund, and Suresh, S., *Thin Film Materials* (Cambridge University Press, 2004).

AUTHOR DECLARATIONS

Conflict of Interest

The authors have no conflicts to disclose.

Author Contributions

Zihan Liu: Formal analysis (lead); Investigation (lead); Writing – review & editing (equal). Yingchun Jiang: Formal analysis (equal); Investigation (equal); Writing – review & editing (equal). Dingli Wang: Formal analysis (equal); Investigation (equal); Writing – review & editing (equal). Junpeng Lai: Investigation (supporting); Writing – review & editing (equal). Huimin Zhou: Investigation (supporting); Writing – review & editing (equal). Jia Deng: Investigation (supporting); Writing – review & editing (equal). Changhong Ke: Conceptualization (Lead); Supervision (Lead); Writing – review & editing (Lead).

DATA AVAILABILITY

The data that support the findings of this study are available from the corresponding author upon reasonable request

Figures and Figure Captions

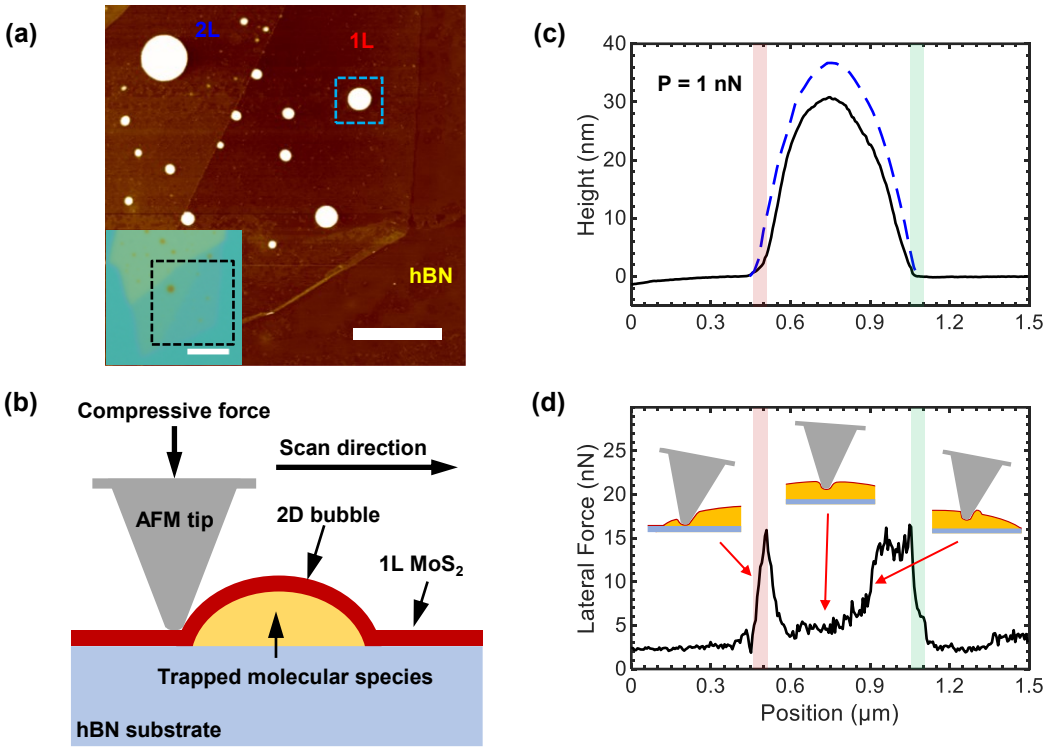

Figure 1: AFM-based nanobubble manipulation: (**a**) AFM image of a MoS_2 flake (with 1L and 2L domains) on a 130-nm thick hBN substrate with simultaneously formed nanobubbles during the dry transfer process. *Scale bar:* 2 μm. The blue dashbox highlights the bubble used for the bubble manipulation experiment. *Insert:* optical microscopy image of the stacked MoS_2/hBN heterostructure. *Scale bar:* 5 μm. (**b**) Schematic of the 2D bubble manipulation on a flat hBN substrate using lateral force AFM. (**c**) The original height profile of the bubble inside the dashbox in (a) (dashed blue curve) using non-contact mode AFM imaging. The contact-mode AFM topographic profile (black curve) under an applied normal load of 1 nN. (**d**) The corresponding AFM lateral force under an applied normal load of 1 nN. *Inset*: schematics of the AFM tip-bubble interaction at different positions. The red and green shaded areas in (c) and (d) indicate the starting and ending stages in the AFM tip-bubble contact, respectively.

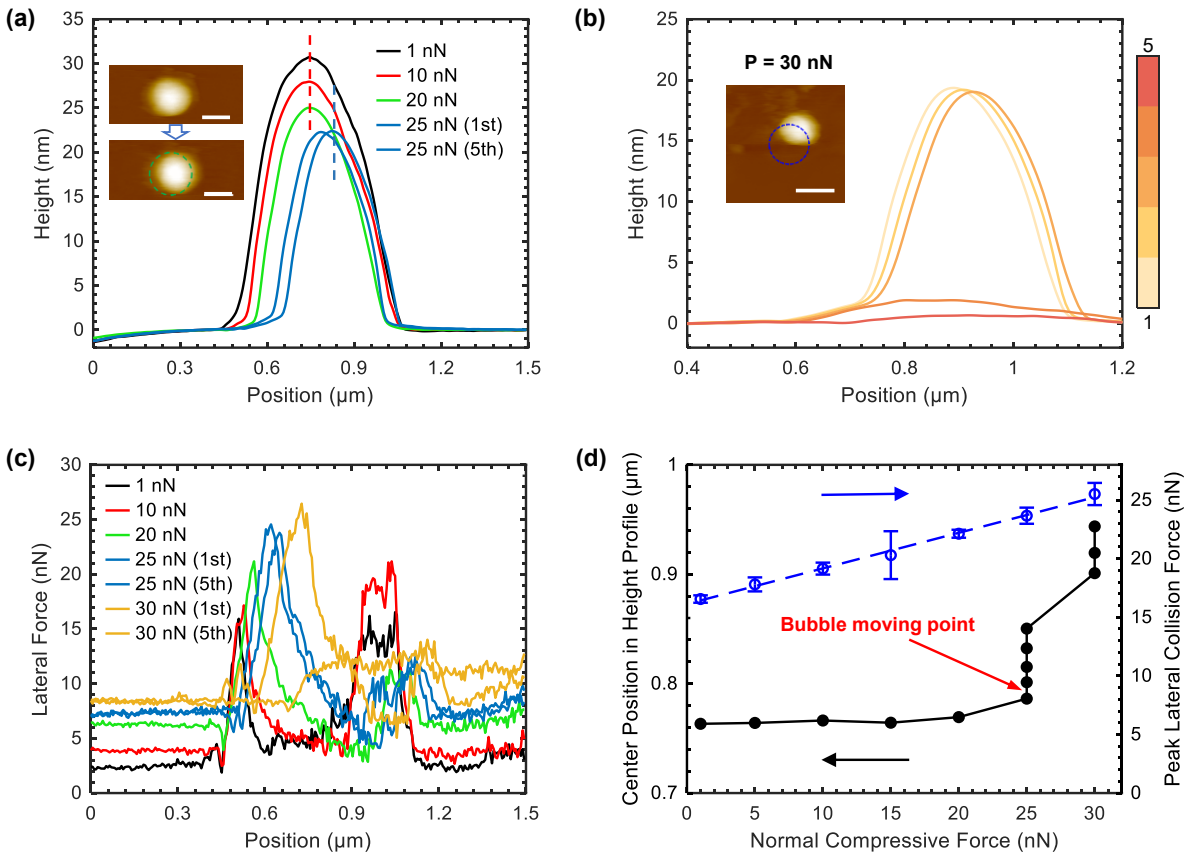

Figure 2: Nanobubble manipulation under varying compressive loads: **(a)** Selected AFM line-scan height profiles of the chosen MoS_2 bubble under each applied normal load (1 nN to 25 nN). The insert AFM images show the bubble's shape and position before and after the first AFM tip scan under a normal load of 25 nN (green dashed circle indicates the original bubble shape/position). **(b)** AFM line-scan height profiles during the five scans under a normal load of 30 nN. The insert AFM image displays the bubble's initial (blue dashed circle) and final shape/positions after the scan cycles under a normal load of 30 nN. The color bar represents the scan sequence. **(c)** Selected lateral collision force profiles for the selected bubbles from 1 nN to 30 nN. **(d)** Evolution of the bubble's central position after each AFM scan and the peak collision lateral force under an increasing normal load at a scan speed of 500 nm/s. Error bars were calculated as the standard deviation of the measured peak lateral forces. *Scale bars* in (a) and (b): 500 nm.

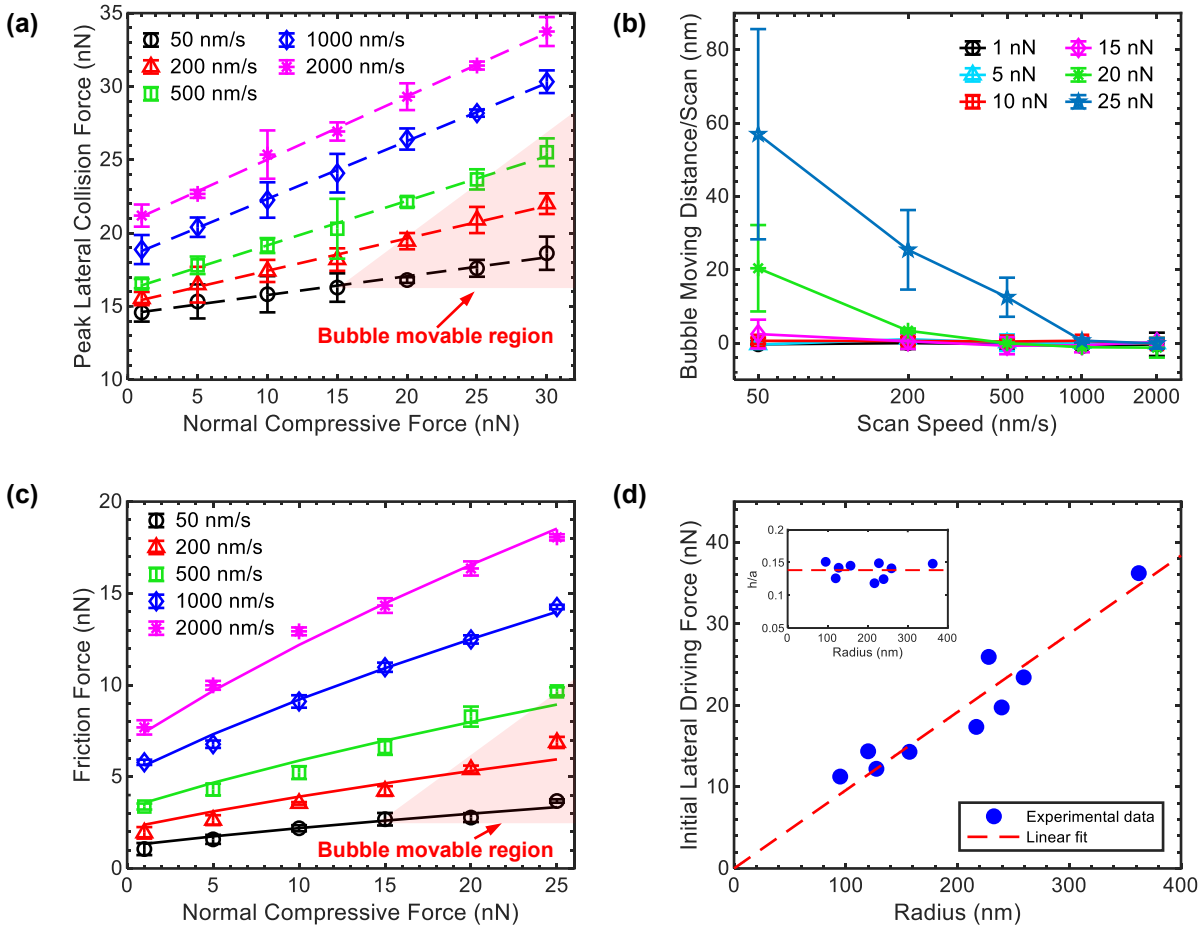

Figure 3: The movability of nanobubbles under varying normal load and AFM tip scan speed: (**a**) The dependency of the peak lateral collision force on the normal load for varying AFM scan speeds. (**b**) Bubble moving distance per scan under applied normal force that ranges from 1 nN to 25 nN at varying scan speeds. (**c**) The dependence of the frictional force on the scan velocity and the applied normal load. (**d**) The measured initial lateral driving force enables the motion of bubbles of varying radii at a scan speed of 500 nm/s. The insert plot shows the aspect ratios of those measured bubbles. Error bars were calculated as the standard deviations of the measured parameters. The red shaded areas in (a) and (c) indicate the bubble's movable domains.

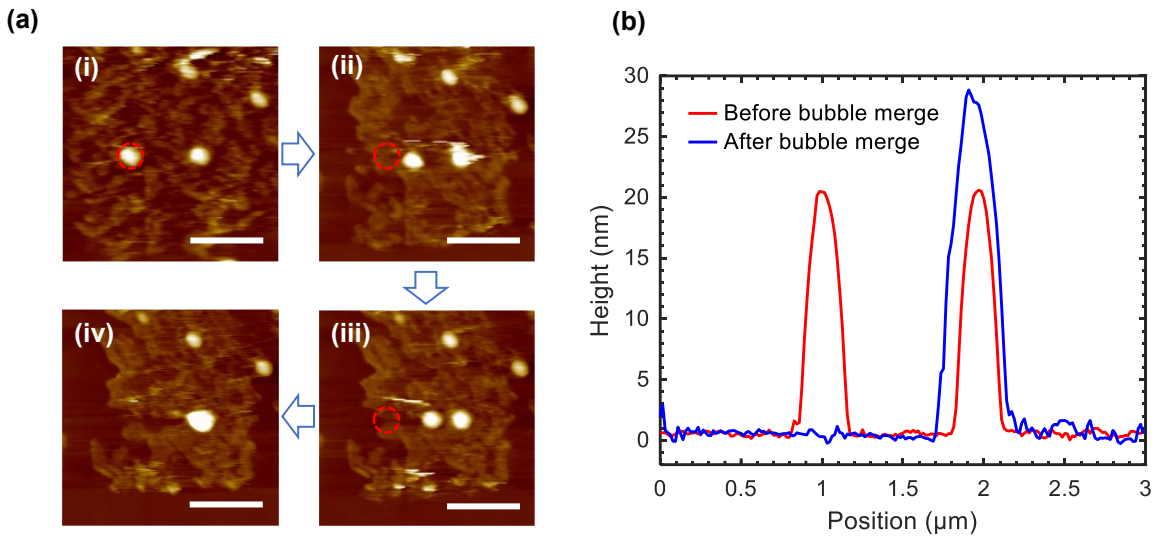

Figure 4: AFM-based nanobubble merging experiments: (**a**) selected AFM snapshots that show the process of merging two nanobubbles into a larger nanobubble. The red dashed circle indicates the original position of the bubble being pushed by the AFM tip. *Scale bar*: 1 μm. (**b**) Height profiles of bubbles before (red line) and after (blue line) the merging process.